



Thickness-dependent ferroelectric and dielectric behaviors for Ni-doped $\text{Na}_{0.05}\text{Bi}_{0.05}\text{TiO}_3$ film derived by chemical solution deposition

X. S. Sun¹ · C. H. Yang¹ · Y. J. Han¹ · J. Chen¹

Received: 7 February 2018 / Accepted: 24 April 2018 / Published online: 30 April 2018
© Springer Science+Business Media, LLC, part of Springer Nature 2018

Abstract

$\text{Na}_{0.05}\text{Bi}_{0.05(1+0.03)}\text{Ti}_{0.97}\text{Ni}_{0.03}\text{O}_3$ (NBTNi) thin films with thickness within the range of 250–880 nm were grown on indium tin oxide (ITO)/glass substrates via a chemical solution deposition method. The thickness impacts on the microstructure, insulating, ferroelectric and dielectric characteristics were investigated. Single perovskite structure in each film is observed from X-ray diffraction. Compared with the other films, the 880 nm-thick NBTNi film has elevated ferroelectric properties with a large remanent polarization (P_r) value of $20.2 \mu\text{C}/\text{cm}^2$ due to the decreased leakage current density resulting from the increasing thickness as well as the large grain size. Moreover, the NBTNi film of 880 nm possesses enhanced energy storage performance with a relatively high energy-storage density value of $45.1 \text{ J}/\text{cm}^3$ and energy-storage efficiency of 37%. Also, a large dielectric tunability value of 25.4% can be obtained at 500 kV/cm and 50 kHz. In addition, the dielectric constant and dissipation factor of the NBTNi film with thickness of 880 nm are 450 and 0.02 at 50 kHz, respectively.

1 Introduction

Ferroelectrics have unique functional properties with applications ranging from sensors, actuators, tunable varactors, phase shifters to ultrasonic transducers [1–3]. Among these ferroelectric materials, sodium bismuth titanate $\text{Na}_{0.5}\text{Bi}_{0.5}\text{TiO}_3$ (NBT), which is a lead-free material with relatively large remanent polarization ($P_r = 38 \mu\text{C}/\text{cm}^2$) and high Curie temperature ($T_c = 320 \text{ }^\circ\text{C}$), has attracted much attention after being synthesized by Smolenskii et al. in 1960 [4, 5]. Low-dimensional materials with high performance have the advantage of overcoming the size effect when comparing with the conventional bulk materials, which is promising to meet the demand of electronic miniaturization [6]. However, for pure NBT in the form of thin film, it has poor electric properties due to the high conductivity [7].

At present, great efforts have been focused on to improve the performance of NBT-based materials. Generally, ions substitution on B-site is supposed to be a serviceable way to reduce the leakage current within a certain degree. Wu et al. have demonstrated that 6 mol% Mn^{2+} -doped ($\text{Na}_{0.85}\text{K}_{0.15}$) $_{0.5}\text{Bi}_{0.5}\text{TiO}_3$ thin film has improved dielectric

property, in which the value of dielectric constant and dielectric loss are 492 and 0.051, respectively [8]. Our previous work has found that NBT film with 3 mol% Ni^{2+} substitution exhibits enhanced ferroelectricity with $P_r = 16.5 \mu\text{C}/\text{cm}^2$ and improved dielectric tunability of 21.7% [9]. Therefore, the 3 mol% Ni^{2+} -doped NBT thin film serves as research object.

Among numerous factors impacting on the properties of the films such as film thickness, annealing atmosphere, annealing temperature and so on, film thickness is a crucial factor affecting the performance of thin films. In the light of this, in order to obtain the high-performance film and make the good compatibility for practical applications, researchers have been paying increasing attention to the film thickness. For instance, Hussain et al. have reported that the leakage current can be reduced by three orders of magnitude as the BeFeO_3 film thickness increases from 40 to 335 nm, leading to improved ferroelectric properties for thicker films [10]. Yu et al. have found the excellent ferroelectricity with a high remanent polarization ($P_r = 61.7 \mu\text{C}/\text{cm}^2$) as well as a low coercive field ($E_c = 70.7 \text{ kV}/\text{cm}$) for 300 nm in Nb-doped $\text{Pb}(\text{Zr},\text{Ti})\text{O}_3$ thin film [11]. The enhanced energy storage density of $6.5 \text{ J}/\text{cm}^3$ at 400 kV/cm can also be achieved in 0.8 μm -thick $(\text{Pb},\text{La})(\text{Zr},\text{Sn},\text{Ti})\text{O}_3$ film [12].

For the preparation of NBT-based films, chemical solution deposition (CSD) can be a favorable choice due to the advantages of good chemical homogeneity and ease of stoichiometric control. In this work, $\text{Na}_{0.05}\text{Bi}_{0.05(1+0.03)}\text{Ti}_{0.97}\text{Ni}_{0.03}\text{O}_3$

✉ C. H. Yang
yang_changhong@163.com

¹ School of Materials Science and Engineering, University of Jinan, Jinan 250022, China

(NBTNi) thin films with various thicknesses from 250 to 880 nm were deposited on indium tin oxide (ITO)/glass substrates by CSD. It was found that the NBTNi film of 880 nm has enhanced ferroelectric and dielectric properties with a large remanent polarization (P_r) of 20.2 $\mu\text{C}/\text{cm}^2$ as well as a large dielectric tunability of 25.4%.

2 Experimental

NBTNi thin films with different thicknesses of 250, 300, 650 and 880 nm (abbreviated as NBTNi-250, NBTNi-300, NBTNi-650 and NBTNi-880) were prepared on ITO/glass using the CSD process. The detailed preparation process of precursor solution was as follows. Firstly, sodium acetate, bismuth nitrate, titanium isopropoxide and nickel acetate tetrahydrate were selected as raw materials dissolved in a mixture of acetic acid and ethylene glycol for preparing the precursor solution. 30% by weight of polyethylene glycol was added to stabilize the precursor. And 3 mol% excess of bismuth nitrate was added to make up the bismuth loss in the annealing process. Meanwhile, appropriate amount of titanium isopropoxide was added in acetylacetone. Then, mixing these two solutions and stirring to produce a transparent and stable precursor solution with the molar concentration of 0.3 M. For each film, the precursor solution was deposited onto ITO/glass substrate via spin coating and then preheated to remove organic solvent on the hot plate at 250 °C for 5 min. Each layer of film was annealed in the air at 550 °C for 10 min by rapid thermal annealing. The processes were repeated several times to achieve an ideal thickness.

The crystal structure of NBTNi thin films was examined by an X-ray diffractometer (XRD, Bruker D8). The surface and cross-sectional morphologies of the films were observed using a field-emission-scanning electron microscope (FeSEM, Hitachi S-4200). In order to evaluate the electrical properties, the structures of Au-NBTNi-ITO have been formed by a sputtering system. The insulating and ferroelectric properties were examined through a standard ferroelectric tester (Precision Pro. Radiant Technologies). And an impedance analyzer (HP4294A) was utilized to measure the dielectric behaviors.

3 Results and discussion

Figure 1 shows the XRD spectra of the NBTNi thin films with different thicknesses ranging from 250 to 880 nm. The NBTNi films are indexed with reference to the rhombohedral structure of NBT ceramics. One can note that each film has the single perovskite structure without any impurity peaks, which could be attributed to the following three factors: (1) The high uniformity of the precursor solution. (2) The

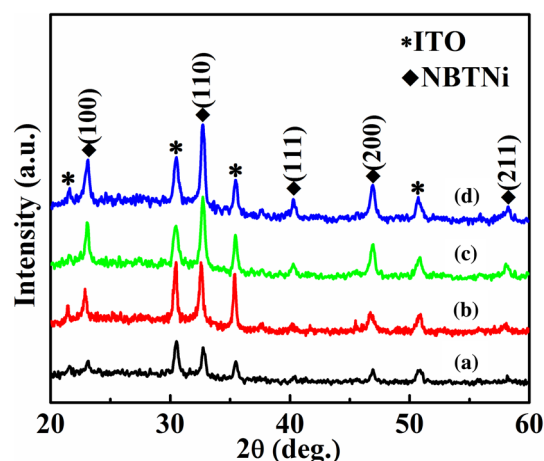


Fig. 1 XRD patterns of NBTNi thin films with different thicknesses: **a** 250 nm, **b** 300 nm, **c** 650 nm and **d** 880 nm

favorable contribution of oxide substrate to nucleation and growth of thin films. (3) The Ni-doping amounts within the doping limit of Ni ions [9]. Moreover, the sharper (110) diffraction peak can be found with the thickness increasing. And the values of full width at half-maximum (FWHM) of (110) diffraction peak for NBTNi-250, NBTNi-300, NBTNi-650 and NBTNi-880 films are 0.369, 0.367, 0.361 and 0.356, respectively, indicating that the grain size increases as the thickness raises according to the Scherrer formula [13].

The surface and cross-sectional images of the NBTNi thin films with different thicknesses are shown in Fig. 2. It can be seen that all the films have some randomly scattered pinholes caused by the volatilization of organic substances when conducting annealing treatment, which is inevitable during the process of pyrolysis and crystallization. In our study, we analyse the size distribution of each film using an image analysis software (Nano Measurer 1.2) [14], and the grain size distributions can be seen in Fig. 3. The average grain size for the films with thickness of 250, 300, 650, 880 nm are 36, 48, 76 and 112 nm, respectively. Such variation tendency that the grain size increases as the thickness raises can be also observed in the thin films of BiFeO_3 and $\text{PbZr}_{0.52}\text{Ti}_{0.48}\text{O}_3$ [15, 16]. According to the cross-sectional images, the thicknesses of the samples are within the range of 250~880 nm. One can see that all the interfaces between films and substrates are obvious, which suggests the well-coated NBTNi films on the ITO/glass substrates and relatively low ion diffusion.

Figure 4 shows the insulating characteristics of NBTNi thin films with various thicknesses. As the electric field (E) increases, the leakage current density (J) of each film increases monotonically. This could be explained as follows. When Ni substitutes Ti-site, the defect of Ni_{Ti}'' will be formed, which can be combined with V_{O}'' to form defect dipole of $\text{Ni}_{\text{Ti}}''-\text{V}_{\text{O}}''$. At low E , it is difficult for oxygen

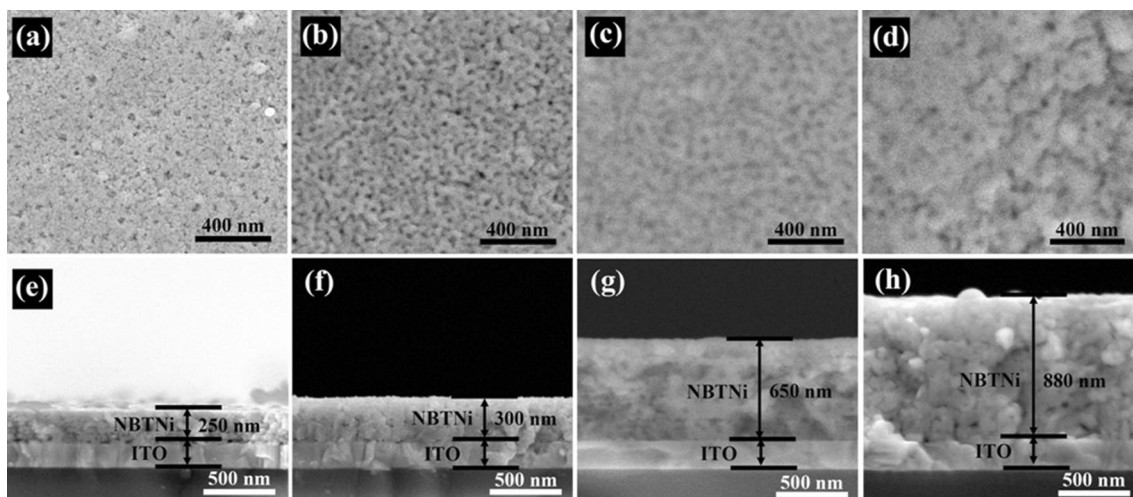
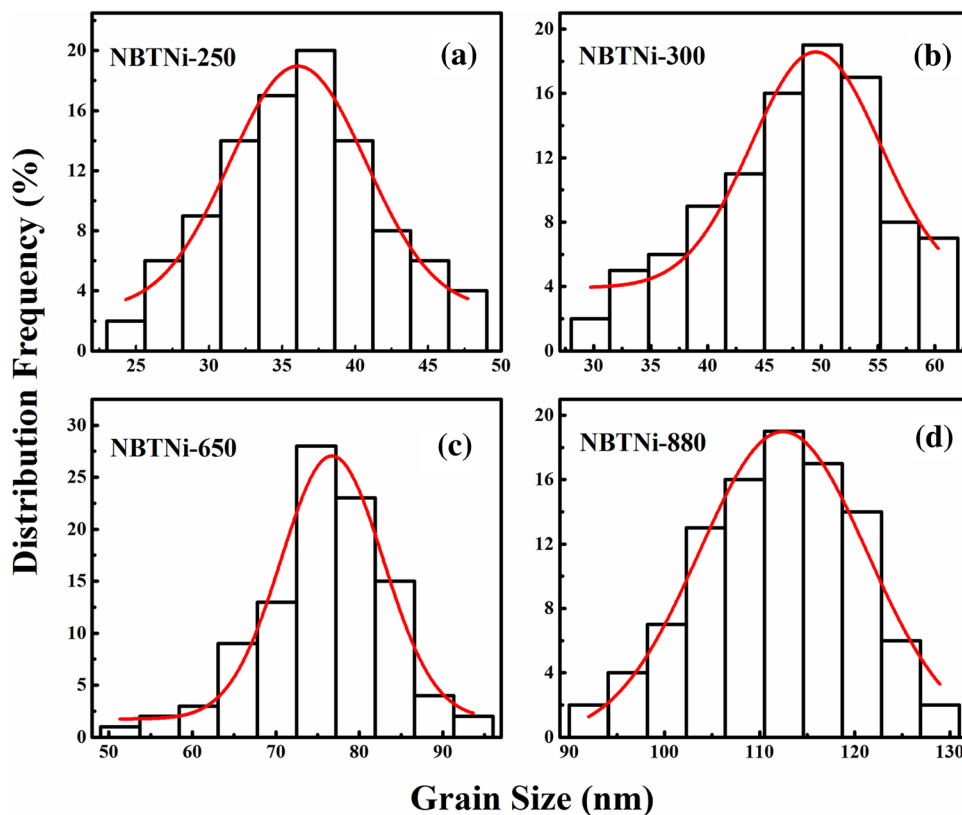


Fig. 2 Surface morphologies and cross-sectional images of NBTNi films with different thicknesses

Fig. 3 Grain size distributions of **a** NBTNi-250, **b** NBTNi-300, **c** NBTNi-650, **d** NBTNi-880 thin films, respectively



vacancies to be released from the defect dipoles because of the electrostatic attraction force. Nevertheless, under high E , more defect dipoles can be broken, leading to an increase of mobile oxygen vacancies, which contributes to the increased J in the films. Moreover, one can note that at a given electric field, the J exhibits a decreasing tendency as film thickness increases, and the J of the NBTNi-880 is at least two orders of magnitude lower than that

of the NBTNi-250 thin film at 500 kV/cm. This may be explained from the following two aspects. (1) The carriers in the thicker film have more difficulty reaching the electrodes due to the longer migration distance [17]. (2) Gradually, the large grain size has small volume fraction of grain boundary, resulting in fewer defects accumulating at the grain boundaries. The experimental results indicate that the insulating property of NBT-based film could be

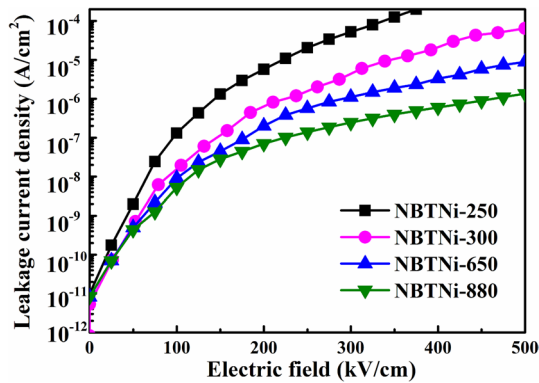


Fig. 4 Leakage current density as a function of electric field for NBTNi thin films with thickness increasing from 250 to 880 nm

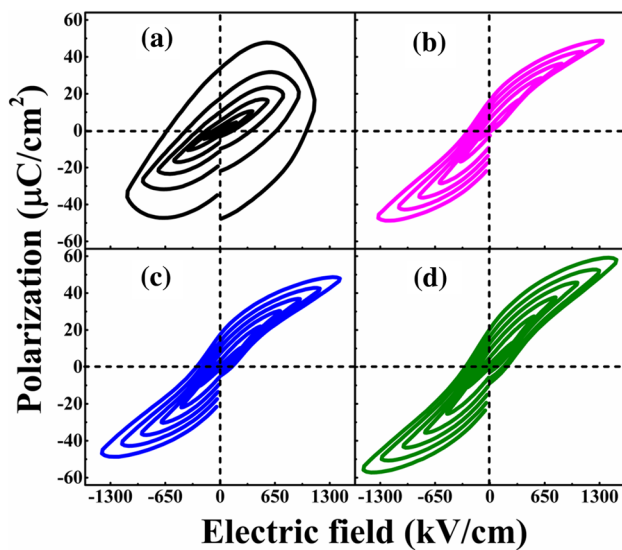


Fig. 5 The P - E hysteresis loops of NBTNi films with different thicknesses: **a** 250 nm, **b** 300 nm, **c** 650 nm and **d** 880 nm

effectively improved through appropriately increasing the thickness of thin film.

Figure 5 presents the polarization-electric field (P - E) hysteresis loops of NBTNi films with the thickness ranging from 250 to 880 nm. Here, the maximum E is the peak value that the film can withstand. The NBTNi-250 thin film takes on poor P - E loops with round shape, indicating the severe electric leakage in film. So the “huge” polarization observed in Fig. 5a mainly originates from the charge injection and space charge contribution. The similar phenomenon can also be found in the BiFeO₃ film [18]. On the contrary, the other three NBTNi films present obvious slim P - E loops, indicating the improved insulating property with the thickness increasing. The enhanced polarization can be obtained in the NBTNi-880 thin film with a large P_r value of 20.2 $\mu\text{C}/\text{cm}^2$, which can be comparable to some

ferroelectric films, such as NBT lead-free ferroelectric thin film prepared by the sol-gel method ($P_r = 8.3 \mu\text{C}/\text{cm}^2$) [19], Na_{0.5}Bi_{0.5}(Ti_{0.98}Mn_{0.02})O₃ thin film derived using CSD ($P_r = 10.2 \mu\text{C}/\text{cm}^2$) [20] and NBT ferroelectric thin film grown by pulsed laser deposition ($P_r = 15.9 \mu\text{C}/\text{cm}^2$) [21]. Note that the P - E hysteresis loops shift toward the negative E axis, which indicates the presence of positive internal field in all films. The different work functions between top Au and bottom ITO electrodes can generate a local field [22]. At the top and bottom interfaces, the space charges may be in asymmetric distribution. When Ni substitutes Ti-site, the defect dipoles of $Ni_{Ti}''-V_O^\bullet$ should not be ignored.

Considering the application of dielectric materials in energy storage, we studied the energy-storage density W and energy-storage efficiency η of the NBTNi films with different thicknesses by following formulas:

$$W = \int_{P_r}^{P_{\max}} EdP$$

$$\eta = \frac{W}{W + W_{\text{loss}}}$$

where E is the applied electric field, P is the polarization, P_r is the remanent polarization and P_{\max} is the maximum polarization. Moreover, W and W_{loss} are energy-storage density and energy loss density, respectively. And the calculated results are shown in Fig. 6. As expected, the W of all the films increases while the η decreases with E increasing. The similar variation trend can be also found in 0.7(Na_{0.5}Bi_{0.5})TiO₃-0.3SrTiO₃ thin films [23]. Among all the samples, the NBTNi-880 film exhibits improved energy-storage performance with $W = 45.1 \text{ J}/\text{cm}^3$ and $\eta = 37\%$ at its critical breakdown electric field strength of 1500 kV/cm, which can be comparable to that of NBT film ($W = 12.4 \text{ J}/\text{cm}^3$, $\eta = 43\%$ at 1200 kV/cm) prepared using a polyvinylpyrrolidone-modified sol-gel technique [24].

The relative dielectric constant (ϵ_r) as a function of E for the NBTNi films with various thicknesses, measured at 500 kV/cm and 50 kHz, are presented in Fig. 7. It can be noted that each ϵ_r - E curve of NBTNi films exhibits the butterfly characteristic with E sweeping according to the measurement mode: $-E$ to $+E$ (the solid symbol), and then $+E$ to $-E$ (the open symbol). The dielectric constant on electric field is strongly nonlinear, confirming the ferroelectric nature of the NBTNi films. All the curves show asymmetric behavior at the negative and positive electric fields, which is coincident with the P - E loops presented in the Fig. 5. Generally, the most noticeable property of ferroelectric films for applying on tunable devices is the dielectric tunability [$T = (\epsilon_0 - \epsilon_{\max})/\epsilon_0$, ϵ_0 and ϵ_{\max} represent

Fig. 6 Electric field dependence of energy-storage density and energy-storage efficiency of thin films with different thicknesses

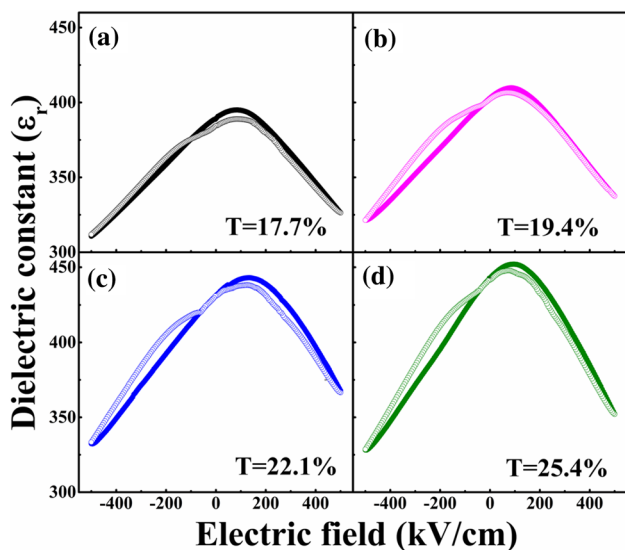
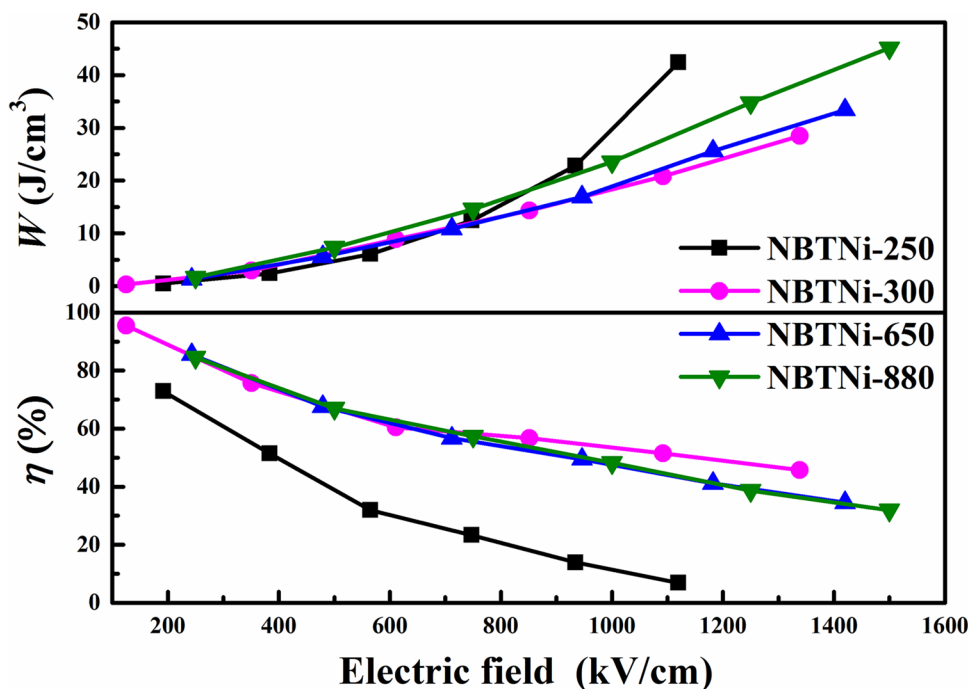


Fig. 7 The ϵ_r - E for NBTNi thin films with different thicknesses: **a** 250 nm, **b** 300 nm, **c** 650 nm and **d** 880 nm

ϵ_r at the intersection point and the maximum negative E , respectively], which can evaluate the ability of ϵ_r variation following with E . The tunability increases as the thickness increases and the maximum value of 25.4% is obtained in NBTNi-880. The result implies that appropriate increase in thickness may be a favorable way to improve the tunability in NBT-based films. Moreover, we can also see the existence of a slight valley in butterfly curves, which indicates that there may be defect dipoles in the films.

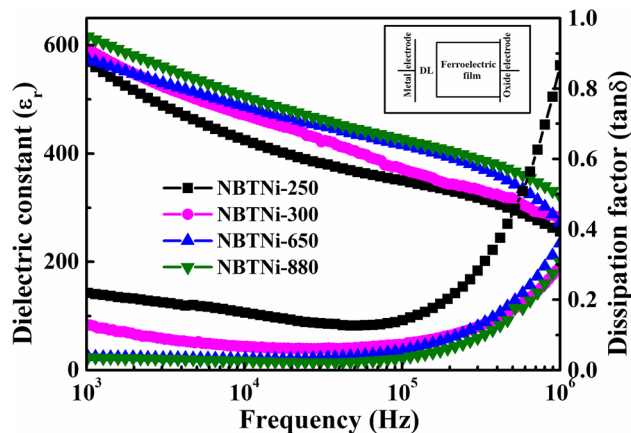


Fig. 8 Frequency dependence of the dielectric constant and dissipation factor for NBTNi thin films with thickness ranging from 250 to 880 nm. The inset is the schematic of the series capacitor structure formed from ferroelectric layer, DL and two electrodes

This feature can be usually found in the aged ferroelectric thin films [23]. For NBT film doped with Ni^{2+} , the defect dipoles of $\text{Ni}_{\text{Ti}}''-\text{V}_{\text{O}}^{**}$ give rise to the aging.

The ϵ_r and dissipation factor ($\tan\delta$) of NBTNi thin films with different thicknesses as functions of operating frequency are measured and displayed in Fig. 8. For all the films, the ϵ_r decreases with increase in frequency, which can be attributed to the polarization processes. At higher frequency, more polarizations have no sufficient time to switch following the changing electric field [25]. Meanwhile, at a certain frequency, the increased ϵ_r can be obtained with the

thickness increasing. This can be explained by that the capacitor structure of Au-NBTNi-ITO exists “dead layer” (DL) at the interface between metal electrode and ferroelectric [26], as shown in the inset of Fig. 8. Generally, ferroelectric layer, DL and two electrodes are in series. The thickness of the interfacial DL can be considered to be independent of the total thickness of film and it is usually assumed that the ϵ_F is much larger than the ϵ_{DL} (ϵ_F and ϵ_{DL} are the permittivity of ferroelectric layer and DL, respectively) [26]. Moreover, according to $\frac{1}{C} = \frac{1}{C_F} + \frac{1}{C_{DL}}$ and

$$C = \frac{\epsilon_r \times \epsilon_0 \times S}{d}, \text{ the formula of } \epsilon_r = \frac{d}{\frac{d-d_{DL}}{\epsilon_F} + \frac{d_{DL}}{\epsilon_{DL}}} \text{ can be obtained,}$$

where C_F is the capacitance of the ferroelectric layer, C_{DL} is the capacitance of the DL, S is the area of the electrode, d is the distance between the top and bottom electrodes, ϵ_0 is the permittivity of vacuum and d_{DL} is the thickness of DL. Consequently, the ϵ_r increases with the film thickness increasing. In addition, the $\tan\delta$ decreases slowly and then increases rapidly as the frequency raises. At lower frequency, $\tan\delta$ is strongly influenced by the space charge polarization effect [27]. And movable space charges are mainly from $V_O^{\bullet\bullet}$, which can lead to high leakage current density [28]. The release of $V_O^{\bullet\bullet}$ can be more and more difficult from the defect dipoles with the increase of frequency, which could decrease the content of $V_O^{\bullet\bullet}$. Hence, the decrease of $\tan\delta$ with increasing the frequency at lower frequency can be obtained. However, at higher frequency, the dipole inertia makes dominant contributions [29]. The similar dependence of ϵ_r and $\tan\delta$ on frequency can also be observed in the $(\text{Na}_{1-x}\text{K}_x)_{0.5}\text{Bi}_{0.5}\text{TiO}_3$ thin film [30]. And for NBTNi-880 thin film, the ϵ_r and $\tan\delta$ values are 450 and 0.02 at 50 kHz, respectively.

4 Conclusion

In summary, we prepared NBTNi thin films with various thicknesses on ITO/glass substrates via CSD successfully. Each film has single perovskite structure. Among them, the NBTNi-880 film has enhanced ferroelectric properties with a large P_r value of $20.2 \mu\text{C}/\text{cm}^2$ and energy storage performance with a relatively large W value of $45.1 \text{ J}/\text{cm}^3$ as well as η value of 37%. In addition, NBTNi-880 film has a large dielectric tunability of 25.4% under 500 kV/cm and 50 kHz. The ϵ_r and $\tan\delta$ of NBTNi-880 film are 450 and 0.02 at 50 kHz, respectively.

Acknowledgements This work was supported by Shandong Provincial Natural Science Foundation of China (ZR2017LEM008) and the National Key R&D Program of China (Grant no. 2016YFC0701005).

References

1. T. Pecnik, S. Glinsek, B. Kmet, B. Malic, J. Alloys Compd. **646**, 766–772 (2015)
2. D.X. Yan, L.Z. Luo, Y.B. Zhang, Z.H. Peng, H. Liu, D.Q. Xiao, T.W. Liu, X.C. Lai, J.G. Zhu, Ceram. Int. **41**, S520–S525 (2015)
3. X. Liu, J.W. Zhai, B. Shen, F. Li, Y. Zhang, P. Li, B.H. Liu, J. Eur. Ceram. Soc. **37**, 1437–1447 (2017)
4. Z. Fu, R.Q. Zhu, D. Wu, A.D. Li, J. Sol–Gel. Sci. Technol. **49**, 29–34 (2009)
5. Y.C. Guo, H.Q. Fan, C.B. Long, J. Shi, L. Yang, S.H. Lei, J. Alloys Compd. **610**, 189–195 (2014)
6. Y.Q. Dai, J.M. Dai, X.W. Tang, K.J. Zhang, X.B. Zhu, J. Yang, Y.P. Sun, J. Alloys Compd. **587**, 681–687 (2014)
7. C.H. Yang, H.T. Sui, G. Wang, F.J. Geng, C. Feng, Ceram. Int. **41**, 859–863 (2015)
8. Y.Y. Wu, X.H. Wang, C.F. Zhong, L.T. Li, J. Am. Ceram. Soc. **94**, 3877–3882 (2011)
9. C.H. Yang, J. Qian, Y.J. Han, X.S. Sun, Z.Y. Sun, L.X. Chen, Ceram. Int. **44**, 7245–7250 (2018)
10. S. Hussain, S.K. Hasanain, G.H. Jaffari, S.I. Shah, Curr. Appl. Phys. **15**, 194–200 (2015)
11. Q. Yu, J.F. Li, W. Sun, Appl. Surf. Sci. **265**, 334–338 (2013)
12. Q.L. Zhao, H. Lei, G.P. He, J.J. Di, D.W. Wang, P.P. Tan, H.B. Jin, M.S. Cao, Ceram. Int. **42**, 1314–1317 (2016)
13. H.L. Dong, L.X. Li, S.H. Yu, Y.X. Jin, D. Xu, J. Alloys Compd. **622**, 79–85 (2015)
14. M.D. Li, M. Hu, Q.L. Liu, S.Y. Ma, P. Sun, Appl. Surf. Sci. **268**, 188–194 (2013)
15. X.W. Tang, J.M. Dai, X.B. Zhu, J.C. Lin, Q. Chang, D.J. Wu, W.H. Song, Y.P. Sun, J. Am. Ceram. Soc. **95**, 538–544 (2012)
16. J.P.D.L. Cruz, E. Joanni, P.M. Vilarinho, A.L. Kholkin, J. Appl. Phys. **108**, 114106 (2010)
17. C.J. Chen, J.N. Ding, J.H. Qiu, N.Y. Yuan, Mater. Lett. **139**, 325–328 (2015)
18. X.D. Qi, J. Dho, R. Tomov, M.G. Blamire, J.L. MacManus-Driscoll, Appl. Phys. Lett. **86**, 062903 (2005)
19. T. Yu, K.W. Kwok, H.L.W. Chan, Thin Solid Films **515**, 3563–3566 (2007)
20. C. Feng, C.H. Yang, Y.Y. Zhou, F.J. Geng, P.P. Lv, Q. Yao, J. Alloys Compd. **679**, 133–137 (2016)
21. J.R. Duclere, C. Cibert, A. Bouille, V. Dorcet, P. Marchet, C. Champeaux, A. Catherinot, S. Deputier, M.G. Viry, Thin Solid Films **517**, 592–597 (2008)
22. C.H. Yang, Y.J. Han, X.S. Sun, J. Chen, J. Qian, L.X. Chen, Ceram. Int. **44**, 6330–6336 (2018)
23. Y.L. Zhang, W.L. Li, W.P. Cao, Y. Feng, Y.L. Qiao, T.D. Zhang, W.D. Fei, Appl. Phys. Lett. **110**, 243901 (2017)
24. Y. Zhao, X.H. Hao, M.L. Li, J. Alloys Compd. **601**, 112–115 (2014)
25. Y.J. Ren, X.H. Zhu, C.Y. Zhang, J.L. Zhu, J.G. Zhu, D.Q. Xiao, Ceram. Int. **40**, 2489–2493 (2014)
26. B. Chen, H. Yang, L. Zhao, J. Miao, B. Xu, X.G. Xin, B.R. Zhao, Appl. Phys. Lett. **84**, 583 (2004)
27. A. Saxena, P. Sharma, A. Saxena, V. Verma, R.S. Saxena, Ceram. Int. **40**, 15065–15072 (2014)
28. Z.X. Cheng, X.L. Wang, S.X. Dou, H. Kimura, K. Ozawa, J. Appl. Phys. **104**, 116109 (2008)
29. M. Cheng, G.Q. Tan, X. Xue, A. Xia, H.J. Ren, Phys. B-Condens. Matter. **407**, 3360–3363 (2012)
30. K. Zhan, X.J. Zheng, J.F. Peng, Y.K. Zhu, H.B. Cheng, Ceram. Int. **41**, 3474–3480 (2015)